ADVANCED FUNCTIONAL MATERIALS
www.afm-journal.de

Tracking Twin Boundary Jerky Motion at Nanometer and Microsecond Scales

Emil Bronstein, László Zoltán Tóth, Lajos Daróczi, Dezsö László Beke, Ronen Talmon, and Doron Shilo*

The jerky motion of twin boundaries in the ferromagnetic shape memory alloy Ni-Mn-Ga is studied by simultaneous measurements of stress and magnetic emissions (ME). A careful design of the experimental conditions results in an approximately linear relationship between the measured ME voltage and the nm-scale volumes exhibiting twinning transformation during microsecond-scale abrupt "avalanche" events. This study shows that the same distributions of ME avalanches, related to features of jerky twin boundary motion, are found both during and between stress drop events. Maximum likelihood analysis of statistical distributions of several variables reveals a good fit to power laws truncated by exponential functions. Interestingly, the characteristic cutoffs described by the exponential functions are in the middle of the distribution range. Further, the cutoff values can be related to the physical characteristics of the studied problem. Particularly, the cutoff of amplitudes of ME avalanches matches the value predicted by high rate magnetic pulse tests performed under much larger driving force values. This observation implies that avalanches during slow rate twin boundary motion and velocity changes observed by high rate tests represent the same behavior and can be described by the same theory.

1. Introduction

Twinning is an essential mode of plastic deformation occurring via nucleation and motion of twin boundaries.[1,2] This process governs the mechanical behavior of a variety of solid materials, such as hexagonal close-packed (HCP) metals (e.g., Mg and Ti),[1] nano-crystalline and nano-structures of face-centered cubic (FCC) metals (e.g., Cu and Ni),[3–5] and nano-structures of ceramic materials (e.g., zirconia).[6] Additionally, twinning reorientation in ferroelastic oxide crystals is the main mechanism responsible for seismic wave attenuation in Earth's lower mantle.[7] Twinning reorientation in ferroelectric materials, shape memory alloys (SMA) and ferromagnetic SMA (FSMA) facilitates significant straining,[8] thus providing the fundamental mechanisms for transformation between electric/magnetic/thermal energy and mechanical energy, which are used in a variety of advanced actuation, sensing and energy harvesting applications.[9–12]

When driven at slow rates, twin boundaries propagate in a jerky motion, which is composed of discrete and impulsive events termed "avalanches" that produce crackling noise.[13,14] Studies of twinning induced by mechanical loading[15–17] and external magnetic/electric fields[18–20] often reported avalanche distributions that follow a power law. This observation is commonly interpreted as an indication for dynamic criticality,[13,14] a state that is characterized by unpredicted dynamics that do not follow a continuous and injective kinetic law.

When driven at high rates, twin boundary dynamics in ferroelectrics,[21–23] FSMA,[24–26] Ni,[27] and Mg[28,29] were found to follow kinetic relations that are determined by lattice barriers for the twin boundary motion. Nevertheless, part of the studies have reported a significant scattering of the measured velocities at a given value of the electric or magnetic field,[23–26] indicating that twin boundary dynamics at high rates displays a jerky motion, as well. However, the magnitudes of the jerks are unclear. Some studies of the motion of type II twin boundary in Ni-Mn-Ga have reported small fluctuations of twin boundary velocity about a most probable value determined by a kinetic relation.[26] Other studies of the dynamics of both type I and type II twin boundaries in Ni-Mn-Ga revealed that their velocities are scattered over almost two orders of magnitude.[24,25]

The connection, if any, between avalanches at slow rates and velocity changes at high rates is still unexplored. To study this problem, direct measurements of twin boundary motion at small length and time scales have to be performed. Studies of twin boundary motion at high rates have been performed by tracking their position using optical microscopy.[24,25] This method is limited to detection of twin

E. Bronstein, D. Shilo
Faculty of Mechanical Engineering
Technion - Israel Institute of Technology
Haifa 3200003, Israel
E-mail: emilbr@campus.technion.ac.il
L. Z. Tóth, L. Daróczi, D. L. Beke
Department of Solid State Physics
University of Debrecen
P. O. Box 400, Debrecen H-4002, Hungary
R. Talmon
Viterbi Faculty of Electrical & Computer Engineering
Technion - Israel Institute of Technology
Haifa 3200003, Israel
The ORCID identification number(s) for the author(s) of this article can be found under https://doi.org/10.1002/adfm.202106573.

DOI: 10.1002/adfm.202106573

boundary displacements larger than ≈1 μm and temporal resolution longer than ≈10 μs. Direct measurements of twin boundary motion at slow rates have been performed by force versus time measurements.[26,30] Despite the high resolution and bandwidth of the force sensor applied in these studies, this method is still limited to avalanches longer than ≈1 ms and force drops that correspond to twin boundary displacements larger than ≈1 μm.

There are many studies on twinning at slow rates by means of acoustic emission (AE) measurements, which are much more sensitive to avalanches occurring at small scales.[17,20,31] However, the relations between measured AE signals and avalanche characteristics that describe the physical process in the material are not clear due to several inherent limitations.[32,33] First, acoustic transducers have a relatively narrow bandpass, typically, between 200 to 900 kHz.[34] As a result, the measured AE signal captures only a small fraction of the overall acoustic energy that is emitted during an avalanche event.[30] Second, the initial acoustic strain change, which corresponds to the actual avalanche and occurs at the μs scale,[35] is modified by the propagation of the acoustic wave within the sample and transducer that typically lasts for 100 μs–10 ms.[34] Third, during this long propagation time, more AE excitations may occur. Several recent works have been trying to cope with the aforementioned limitations, for example, by means of deconvolution.[32,36]

Recently, our group has demonstrated the application of magnetic emission (ME, which is also known as Barkhausen noise) measurements for the study of avalanches occurring during slow rate twinning in the FSMA Ni-Mn-Ga.[18,37,38] The sensitivity of ME measurements to small scale avalanches is comparable to that of AE, but the ME technique does not suffer from the aforementioned inherent limitations of AE. For samples with a small cross-section and using a coil with a small number of windings, a high bandwidth can be obtained and the temporal resolution can go below 1 μs.[18,37,38] Generally, ME measurements capture the overall rate of magnetization change within a (ferromagnetic) sample. Therefore, in principle, this method can provide direct measurements of a moving interface's displacement (e.g., a domain wall) during discrete avalanche events.[39,40] However, this is often not the case due to the complexity of the material behavior that involves several phenomena. For example, magnetization changes in ferromagnetic materials often occur simultaneously via several mechanisms (e.g., 180° domain switching, 90° domain switching, and magnetization rotation) and at several locations within the sample. In FSMA, magnetization changes due to twinning reorientation often couple with magnetization changes due to "ordinary" domain switching.[41] This complexity hinders the ability to relate measured ME events to the motion of a single twin boundary.

In this paper, we study twin boundary motion in the FSMA Ni-Mn-Ga induced by slow compression, during which avalanche events were captured by simultaneous stress drops and ME measurements. The experimental conditions were carefully designed to enable the study of a single twin boundary motion, thus minimizing the complexity of the process that may arise due to motions and interactions of several twin boundaries or due to coupling between twin boundary motion and "ordinary" magnetic domain switching.

Our measurements show that numerous small and rapid ME avalanches occur during each stress drop avalanche, as well as between stress drops. The overall ME during each stress drop is in excellent correlation with the amplitude of the stress drop, indicating that, to a good approximation, the measured ME can be directly related to the motion of the twin boundary (as shown in subsection 3.3). Thus, individual ME events are related to local twin boundary motions at the nanometer and microsecond scales. Further statistical analysis of ME events during stress drops and between stress drops revealed that they are generated by the same process. The only difference between them is found to be the rate of their occurrence, that is, the delay times between consecutive events. Finally, we compare our results with previous studies of twin boundary motion during fast magnetic pulses and provide indications that the same type of jerky behavior occurs both at slow and high rates.

2. Magneto-Mechanical Microstructure of Ni-Mn-Ga

All the experiments described in this work were performed on the same 10M $Ni_{50.0}Mn_{28.5}Ga_{21.5}$ single crystal sample of the dimensions 20 mm × 3 mm × 2.5 mm, produced by AdaptaMat LTD. The experiments were carried out at room temperature, at which the sample is fully at the martensite phase. The unit cell of the 10M martensite is nearly tetragonal, having a small monoclinic distortion,[42] which gives rise to two different types of twin boundaries, type I and type II. Although these two types have almost the same twinning strain $\varepsilon_T \approx 0.06$, their twinning stress is significantly different (0.5–1 MPa for type I and 0.05–0.3 MPa for type II[42,43]). The twin boundaries separate the microstructure into regions (twins) with different orientations of the c-axis of the unit cell, which is also the magnetic easy axis (i.e., the preferred magnetization orientation within the unit cell).

In the absence of an external magnetic field, each twin is divided into 180° magnetic domains, as can be seen in **Figure 1**a. In this configuration, 180° domain switching induces magnetization changes that occur during twin boundary motion but are not related to it. Contrarily, application of a magnetic field in 45° with respect to the axial direction of the sample forms the microstructure illustrated in Figure 1b; namely, a twin boundary that divides the sample into two twins, each with a single magnetization direction.[44] In this configuration, magnetization changes occur (almost) solely due to twin boundary motion. The projection of the magnetic field along the magnetization directions is the same for both twins, resulting in no preference of either of them. Therefore, such orientation of the external magnetic field is not expected to induce twin boundary motion.

Prior to each experiment, the sample is brought to a state at which a single twin boundary is located approximately at the center of the crystal, as illustrated in Figure 1b. Throughout the compression tests, the twin with the magnetization along $\boldsymbol{e}_1$ grows at the expanse of the other twin, while the moving twin boundary is located within the ME sensing coil, as illustrated in Figure 1c. Optical observations, as well as the levels of the plateau

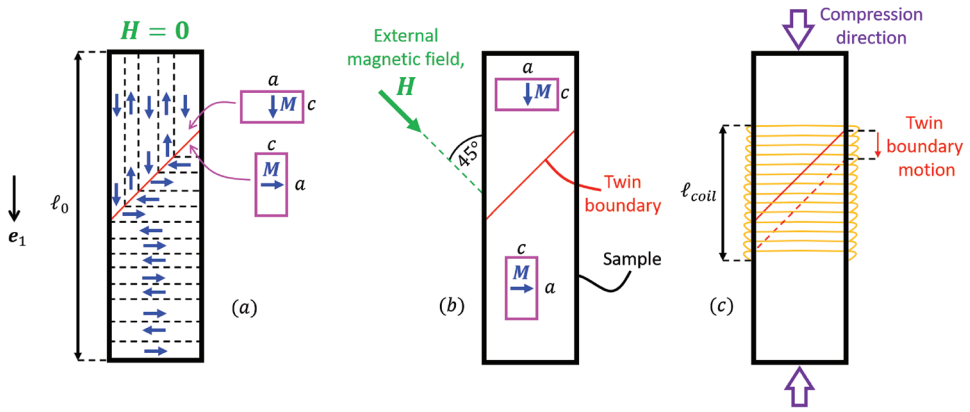

Figure 1. Illustration of the sample in the a) absence and b) presence of an external magnetic field. c) Illustration of the twin boundary motion inside the sensing coil due to compression forces.

stress during the compression tests, imply that the moving twin boundary is of type I. Thereafter, the sample is placed in the magnetic field, such that the microstructural configuration illustrated in Figure 1b is achieved and the sample is ready to be tested.

3. Results

3.1. Force Measurements

A representative stress–time plot, obtained from the force measurements, is shown in **Figure 2** and displays fluctuations about an approximately constant twinning stress. A careful examination of these fluctuations shows that they consist of fast stress drops (big avalanches) separated by moderate stress rise segments. The stress drops have varying amplitudes and timescales. Examples for large ($\Delta\sigma \approx 0.1$ MPa) and relatively fast ($\Delta t \approx 25$ ms), as well as small ($\Delta\sigma \approx 0.02$ MPa) and relatively slow ($\Delta t \approx 220$ ms) stress drops are shown in insets (I) and (II) of Figure 2, respectively. Since the noise level of the stress measurements is 0.003 MPa, we set a threshold of 0.01 MPa, below which stress drops were not considered.

Due to the constant compression rate, c, the strain change $\Delta\varepsilon$ at time interval Δt can be expressed as[44,45]

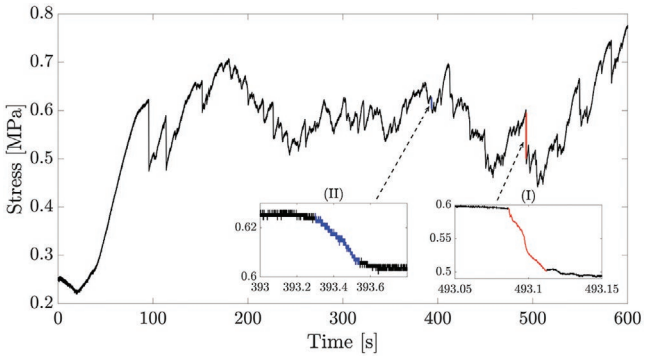

Figure 2. A representative stress–time curve. Inset (I) shows a fast and large stress drop. Inset (II) shows a slow and small stress drop.

$$\Delta\varepsilon = \frac{c\Delta t}{\ell_0} = \frac{\Delta\sigma}{Y} + \frac{V_T}{V_0}\varepsilon_T \tag{1}$$

Here, ℓ_0 is the sample's length, V_0 is the sample's volume, ε_T is the twinning strain, $\Delta\sigma$ is the stress change that corresponds to Δt, V_T is the volume that underwent twinning transformation during the time interval Δt, and Y is the effective elastic modulus determined by the sample and the stiffness of the experimental setup. According to the right-hand-side (RHS) of Equation (1), $\Delta\varepsilon$ is composed of the elastic strain (first term) and the strain change due to the relative volume that underwent twinning transformation (second term).

Equation (1) can be recast as

$$\frac{\Delta\sigma}{\Delta t} = Y\left(\frac{c}{\ell_0} - \frac{V_T}{V_0}\frac{\varepsilon_T}{\Delta t}\right) \tag{2}$$

According to Equation (2), during time intervals in Figure 2 at which the slope increases, the first term on the RHS in Equation (2) is larger than the second term, indicating that V_T is either zero or very small. During fast stress drops, the second term in Equation (2) is larger than the first term, indicating on a discernible transformed volume V_T occurring during this time. Eventually, from Equations (1) or (2), the transformed volumes extracted from force measurements (denoted by V_T^F) are given by

$$V_T^F = \frac{1}{\varepsilon_T}\left(Ac\Delta t - V_0\frac{\Delta\sigma}{Y}\right) \tag{3}$$

where A is the area of the sample's face perpendicular to the compression axis.

3.2. Magnetic Emission Measurements

Figure 3 shows the ME signals during a) a large and fast stress drop, b) a small and slow stress drop, and c) a moderate stress rise. Three interesting observations can be made based on this figure. First, during each stress drop event, there are numerous

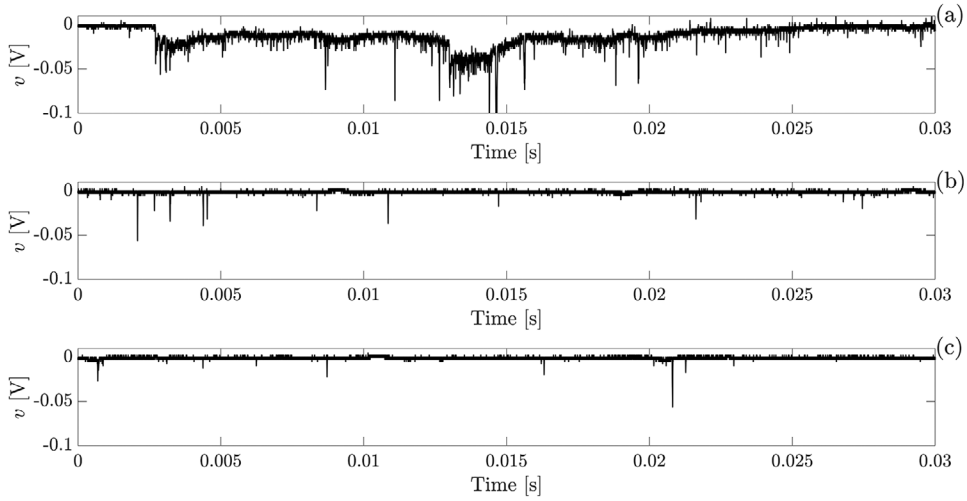

Figure 3. a,b) ME signals corresponding to a) a large and fast and b) to a small and slow stress drops. c) A ME signal captured during a stress rise.

ME avalanche events appearing as sharp rapid voltage bursts with typical durations of less than 50 µs. Second, the ME signal that corresponds to the stress rise (Figure 3c) looks much like the ME signals that correspond to the stress drops (Figure 3a,b). This observation is elaborated and discussed in Section 4. Third, almost all of the ME signal is unidirectional (negative) with respect to zero voltage. This observation strengthens our claim that practically all 180° magnetic domains are annihilated, as otherwise, significant positive ME voltage would be measured as well.

In Figure 3a, the baseline voltage deviates from zero during most of the stress drop. A possible explanation for this effect is that during this large and fast stress drop, there was a small rigid motion of the entire sample, which resulted in an effect similar to that of a permanent magnet moving inside a coil. Such situations are rare in our conducted experiments, but they may result in a wrong detection of ME avalanche events, if not corrected properly. This issue is addressed in Supporting Information.

In the following, we formulate a relation between the ME measurements and the volumes that underwent twinning transformation, V_T, during ME avalanches. According to Faraday's law of induction, the voltage measured at the sensing coil's terminals is given by

$$v = NA\frac{\mathrm{d}\Phi}{\mathrm{d}t} = NA\frac{\mathrm{d}}{\mathrm{d}t}\left(\mu_0\bar{\boldsymbol{M}}\cdot\boldsymbol{e}_1\right) \tag{4}$$

where N is the number of coil turns, $\mathrm{d}\Phi/\mathrm{d}t$ is the rate of change of the magnetic flux through the cross-section area A, μ_0 is the vacuum permeability, $\bar{\boldsymbol{M}}$ is the average sample magnetization and $\boldsymbol{e}_1$ is the longitudinal direction of the sample (see Figure 1). Also

$$\frac{\mathrm{d}}{\mathrm{d}t}\left(\mu_0\bar{\boldsymbol{M}}\cdot\boldsymbol{e}_1\right) = \frac{\mu_0 M_s}{A\cdot\ell_{\mathrm{coil}}}\dot{V}_T \tag{5}$$

where M_s is the spontaneous magnetization of the material ($\mu_0 M_s = 0.65$ T in Ni-Mn-Ga[46,47]) and $\ell_{\mathrm{coil}} \approx 6$ mm is the length of the coil. In Equation (5), $\dot{V}_T$ is the rate of change of volumes undergoing twinning transformation, which results in magnetization change by 90°. Substitution of Equation (5) into Equation (4) and rearrangement of the obtained equation yields

$$\dot{V}_T^{\mathrm{ME}} = \frac{\ell_{\mathrm{coil}}}{N\mu_0 M_s}v \tag{6}$$

As $\dot{V}_T$ is related to ME measurements, we denote it by $\dot{V}_T^{\mathrm{ME}}$.

We wish to emphasize that through Equation (6), our experimental method provides an approximately linear relation between the measured ME voltage, v, and the rate of the twinning transformation, $\dot{V}_T$. Thus, avalanche events (voltage bursts) provide direct information on the studied process (twin boundary motion). The approximation described by Equation (6) is validated in subsection 3.3.

3.3. The Relation between the Force and the Magnetic Emission Measurements

In this subsection, we verify that the transformed volumes calculated by Equation (6) based on the ME signals are in agreement with the transformed volumes calculated by Equation (3) based on the corresponding force measurements. During each stress drop, there are numerous ME events; therefore, we perform the following analysis. First, based on Equation (3), we calculate the transformed volumes from the initial time of a stress drop, t_i, to every sampled point at time, t_n, during the stress drop. That is,

$$V_T^{\mathrm{F}}(t_i, t_n) = \frac{1}{\varepsilon_T}\left(Ac(t_n - t_i) - V_0\frac{\sigma(t_n) - \sigma(t_i)}{Y}\right) \tag{7}$$

Then, based on the ME measurements and by integrating Equation (6), we calculate the same variable (V_T) at the same time interval (from t_i to t_n). Namely

$$V_T^{\mathrm{ME}}(t_i, t_n) = \int_{t_i}^{t_n}\dot{V}_T^{\mathrm{ME}}\mathrm{d}t \tag{8}$$

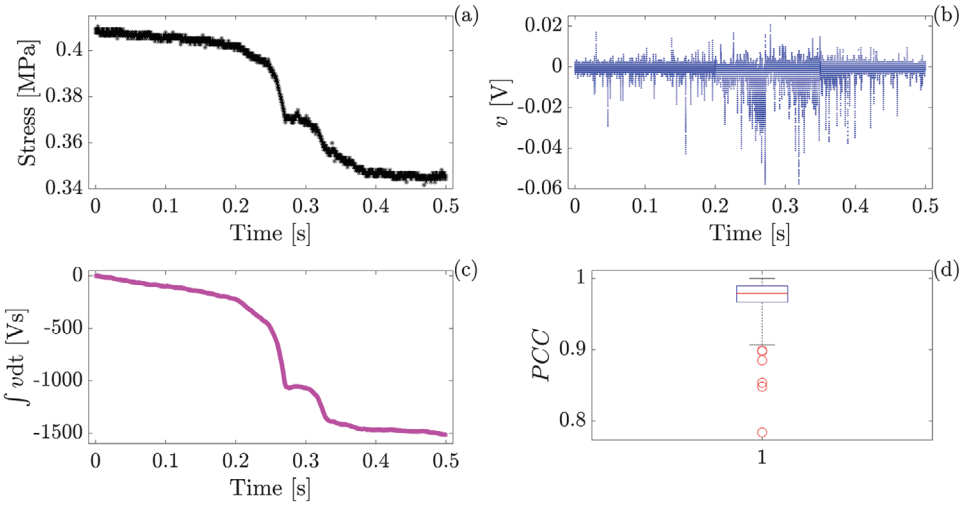

Figure 4. a) A stress drop. b) The ME corresponding to the stress drop in (a). c) Integration of the ME in (b), proportional to Equation (8). d) A boxplot summarizing the statistics of the Pearson correlation coefficients (PCCs) of 216 stress drops. The median is indicated by the central red line, while the bottom and top edges of the blue box indicate the 25th and 75th percentiles, respectively. The PCC values smaller than 0.9 are marked with red circles.

To provide a visualized example for the agreement between V_T^F and V_T^{ME}, we show the stress drop in **Figure 4**a and its corresponding ME (Figure 4b). On the one hand, the time integral of the ME in Figure 4b according to Equation (8), which is shown in Figure 4c, is proportional to V_T^{ME}. On the other hand, the plot in Figure 4a is approximately proportional to V_T^F, as the first term on the RHS of Equation (7) is much smaller than the second term. The similarity between the shapes of the curves in Figure 4a,c, where both are proportional to V_T, implies that Equations (7) and (8) represent the same variable V_T based on different measurements.

We further validate that V_T^F from Equation (7) and V_T^{ME} from Equation (8) are in accordance with each other based on the Pearson correlation coefficients (PCCs). The calculations of PCCs of these measured functions reveal a strong statistical correlation between them, as out of the 216 considered stress drops in nine experiments, over 97% have PCC >0.9 and over 84% have PCC >0.95. The statistics of the PCCs are summarized in a boxplot in Figure 4d.

The aforementioned results indicate that, to a good approximation, the ME measurements represent the volumes that underwent twinning reorientation. Consequently, using our developed experimental method, the jerky motion of the twin boundary can be directly studied at fine scales. Further, since each stress drop avalanche is composed of numerous ME avalanches, the ME measurements provide a large amount of data, which is the focus of the following statistical analysis.

4. Statistical Analysis of Magnetic Emission Avalanches

The analysis of ME signals is based on identifying the onset and end point of each avalanche using the algorithm presented in Supporting Information. For each detected ME avalanche, we compute four variables: $t_{duration}$—the time difference between the onset and end point of the avalanche; $\dot{V}_{T,max}$—the maximal rate of the volume transformation during the avalanche, which is proportional to the maximal absolute value of the voltage during the avalanche; V_T—the transformed volume, calculated by integrating the voltage over the duration time according to Equation (6); t_{delay}—the delay time from an end of an avalanche to the beginning of the consecutive one. We evaluate the statistics of each of the computed variables (V_T, $\dot{V}_{T,max}$, $t_{duration}$, t_{delay}) and present their complementary cumulative distribution functions (CCDFs) in **Figure 5**.

Figure 5 compares the statistical distributions of two subsets of data. The solid red curves represent 40 000 ME avalanches detected during 210 stress drops for which the PCCs calculated in subsection 3.3 are larger than 0.9, indicating on a high certainty of relating the measured ME avalanches to twin boundary motion through Equation (6). The dashed black curves represent 740 000 ME avalanches detected throughout the entire durations of all experiments, containing events that occurred during stress drops, stress rises, and plateau levels of stress. The congruence of the red and black curves of V_T, $\dot{V}_{T,max}$, and $t_{duration}$ over more than 99% of the data indicates that the same microscale processes take place both during and between stress drops. As expected, the curves of t_{delay} in Figure 5d do not coincide, indicating that the delay times between ME avalanches are much shorter during stress drops than during stress plateaux or stress rises. This means that the main feature of a stress drop is the high occurrence rate of microscale avalanches compared to a much lower occurrence rate of these events during other time intervals.

Next, we study the types of the distributions of V_T, $\dot{V}_{T,max}$, and $t_{duration}$ (distributions of t_{delay} are rarely reported in the literature and their analysis is based on different methods[31]). For this purpose, we focus on the data obtained during the entire durations of all experiments, as it is richer than the data obtained only during stress drops and presents approximately the same CCDFs of V_T, $\dot{V}_{T,max}$, and $t_{duration}$. To ensure certainty

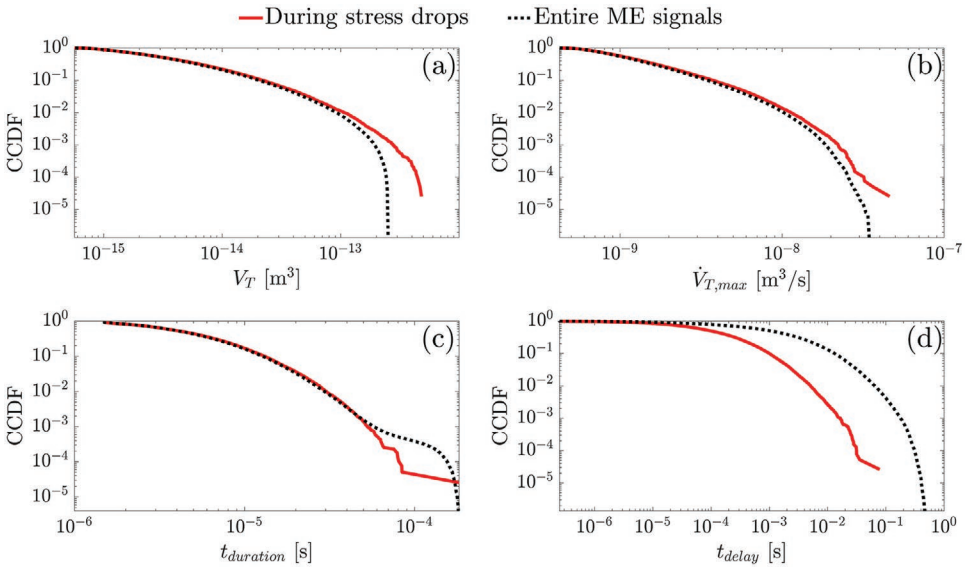

Figure 5. The complementary cumulative distribution functions (CCDFs) of the variables a) V_T, b) $\dot{V}_{T,max}$, c) $t_{duration}$, and d) t_{delay}. The red solid lines denote 40 000 data points obtained during stress drops. The black dashed lines denote 740 000 data points obtained from entire experiments.

of the statistical analysis, we analyze events with $V_T \geq 10^{-15}$ m^3 and $\dot{V}_{T,max} \geq 6.5 \times 10^{-10}$ m^3 s^{-1} (nearly twice the detection capability), which constitutes $\approx 90\%$ of the entire data.

In the following, we apply two statistical analysis approaches, both based on the maximum likelihood method.[48,49] In the first, we search for probability density functions (PDFs) that fit the measured data over the whole analyzed range. We assume that the PDFs, p, follow the commonly observed[50,51] truncated power laws of the forms

$$p(V_T) \propto (V_T)^{-\epsilon} \exp\left(\frac{V_T}{V_T^C}\right) \tag{9}$$

$$p(\dot{V}_{T,max}) \propto (\dot{V}_{T,max})^{-\alpha} \exp\left(\frac{\dot{V}_{T,max}}{\dot{V}_{T,max}^C}\right) \tag{10}$$

$$p(t_{duration}) \propto (t_{duration})^{-\tau} \exp\left(\frac{t_{duration}}{t_{duration}^C}\right) \tag{11}$$

We apply the maximum likelihood method[48,49] for calculating the values of the exponents (ϵ, α, τ) and the cutoffs (V_T^C, $\dot{V}_{T,max}^C$, $t_{duration}^C$) that fit best to the measured data. **Figure 6** shows the CCDFs of the measured data (black curves) and the calculated distributions (magenta curves). The values of the exponents and cutoffs that correspond to the maximum likelihoods are

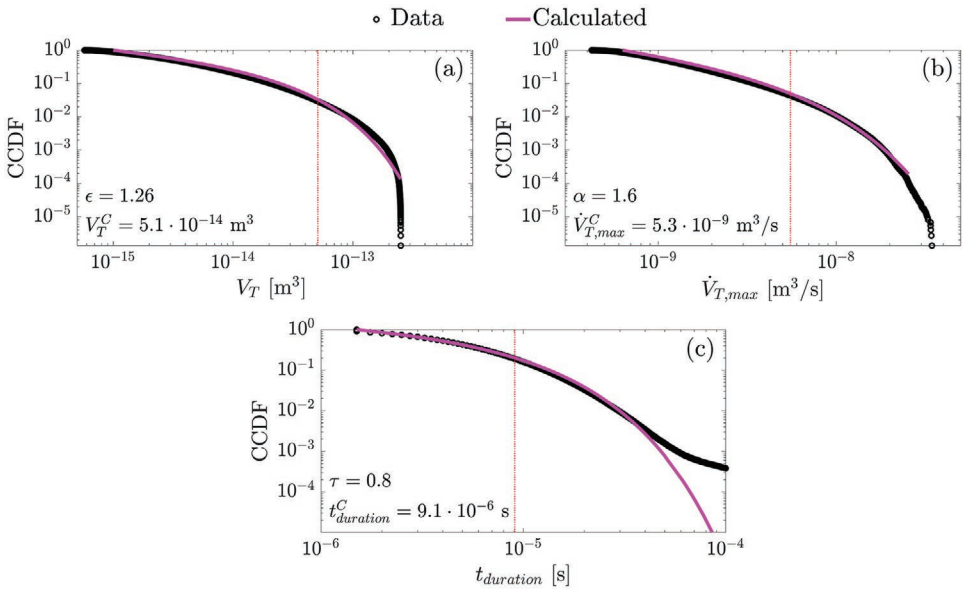

Figure 6. CCDFs of the measured data (black circles) and the calculated (magenta curves) distributions of the variables a) V_T, b) $\dot{V}_{T,max}$, and c) $t_{duration}$ based on Equations (9)–(11). The values of the parameters are indicated in the plots. The red dashed lines show the cutoff values.

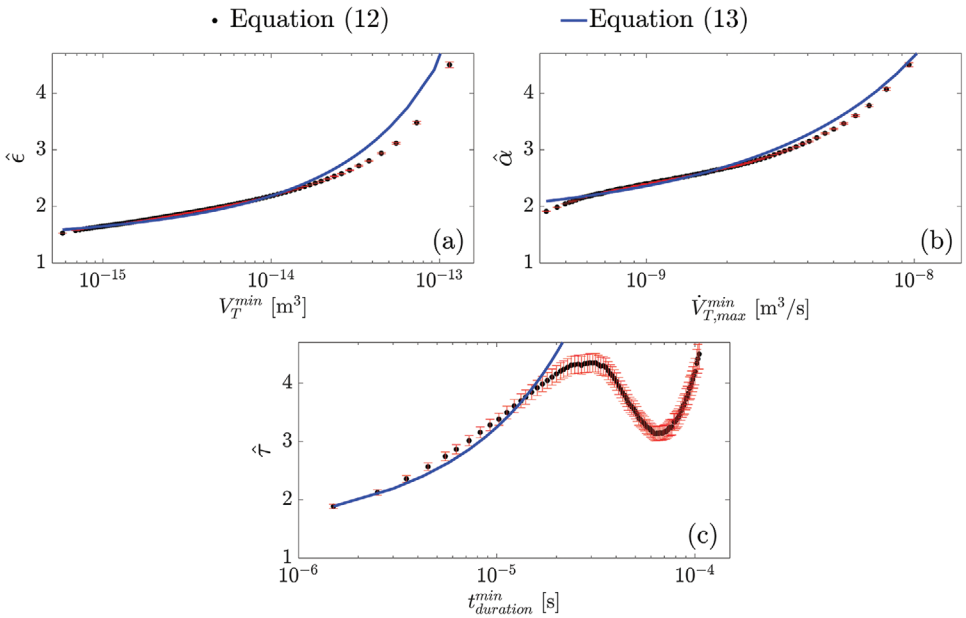

Figure 7. a) $\hat{\epsilon}$ versus V_T, b) $\hat{\alpha}$ versus $\dot{V}_{T,max}$, and c) $\hat{\tau}$ versus $t_{duration}$. The black dots were calculated based on Equation (12) and the blue curves were calculated based on Equation (13). The red error bars are the standard errors.[49,56]

indicated next to the relevant curves. The cutoff values are also marked by the red dashed lines. In Figures 6a– c, the calculated curves fit the measured ones over almost the entire range of the data, but in Figure 6c, for large $t_{duration}$ values, the CCDF of the measured data displays a trend change toward a more heavy-tailed distribution.

In the second analysis approach, we analyze varying segments of the data. Here, we formulate this approach for a general measured variable x, which in our case represents V_T, $\dot{V}_{T,max}$, or $t_{duration}$. Following the method described in ref. [49, 52], we calculate the function

$$\hat{\beta}\left(x^{\min}\right)=1+n\left[\sum_{i=1}^{n}\ln\left(\frac{x_i}{x^{\min}}\right)\right]^{-1} \tag{12}$$

where x_i are the n measured values of x that satisfy $x_i \geq x^{\min}$. For an ideal power law distribution of the form $p(x) \propto x^{-\beta}$ that extends over the whole range of the measured data, $\hat{\beta}$ is the maximum likelihood estimator of the exponent β. In such cases, Equation (12) is expected to satisfy $\hat{\beta}=\beta$ for all values of $x^{\min}$. In practical cases, $\hat{\beta}(x^{\min})$ is not strictly constant, but in many previous studies[14,16,30] such plots displayed a plateau that spanned over a discernible range of the measured data.

For more complicated PDFs, such as truncated power laws or a mixture of power laws, $\hat{\beta}$ is no longer the estimator of the exponent. Nevertheless, the maximum likelihood method enables obtaining analytical expressions for $\hat{\beta}(x^{\min})$, based on which the calculated data of $\hat{\beta}$ versus $x^{\min}$ can be analyzed.[52] In particular, for truncated power law distributions of the form $p(x) \propto x^{-\beta}\exp(-x/x^C)$, such as those described in Equations (9)–(11), $\hat{\beta}$ versus $x^{\min}$ is expected to display a monotonically increasing function expressed by[52]

$$\hat{\beta}\left(x^{\min}\right)=1+\frac{\int_{x^{\min}}^{\infty}x^{-\beta}\exp\left(-x/x^{C}\right)\mathrm{d}x}{\int_{x^{\min}}^{\infty}\ln(x/x^{\min})x^{-\beta}\exp\left(-x/x^{C}\right)\mathrm{d}x} \tag{13}$$

If x^C is very close to the largest measured value, Equation (13) still displays a plateau at a value $\hat{\beta}\approx\beta$ spanning over most of the data range.[52] Yet, Equation (13) predicts cases in which the plot of $\hat{\beta}$ versus $x^{\min}$ does not display a plateau at any segment of the data, and $\hat{\beta}>\beta$ for all values of $x^{\min}$.[52]

We implement the analysis described in Equations (12)–(13) by replacing x and $\hat{\beta}$ with our measured variables V_T, $\dot{V}_{T,max}$, or $t_{duration}$ and their exponent estimators $\hat{\epsilon}$, $\hat{\alpha}$, and $\hat{\tau}$, respectively. **Figure 7** shows plots of $\hat{\epsilon}$, $\hat{\alpha}$. and $\hat{\tau}$ versus the respective minimal values $V_T^{\min}$, $\dot{V}_{T,max}^{\min}$, or $t_{duration}^{\min}$, which replace $x^{\min}$. The analytical predictions represented by the blue curves were calculated using Equation (13) by replacing β and x^C with the maximum likelihood values of the exponents and cutoffs obtained from the analysis of the whole data presented in Figure 6 (i.e., $\epsilon = 1.26$, $\alpha = 1.6$, $\tau = 0.8$, $V_T^C = 5.1\times10^{-14}$ m^3, $\dot{V}_{T,max}^C = 5.3\times10^{-9}$ m^3 s^{-1}, $t_{duration}^C = 9.1\times10^{-6}$ s).

In Figure 7a,b, the monotonic increases of the calculated black dots demonstrate the substantial effects of the exponential contributions to the PDFs expressed by Equations (9)–(10), even in the ranges smaller than the cutoff values. Further, the good agreements of the blue curves with the black dots strengthen the choice of fitting truncated power law functions to the measured PDFs and shows that both methods of data analysis provide the same predictions for the exponent and cutoff values.

In Figure 7c, the blue curve fits the black dots over the majority of the data, but for large $t_{duration}$ values the black dots deviate from the blue curve, reach a local maximum, and then a local minimum. The region in Figure 7c at which the black dots

deviate from the blue curve approximately coincides with the region of large $t_{duration}$ values in Figure 6c, at which the measured CCDF displays a trend change. The shape of the curve formed by the black dots in Figure 7c might be an indication for a combination of two power laws and an exponential truncation, similar to the case-study discussed in ref. [52]. At the moment, there is no mathematical framework to verify this conjecture.

The exponent values $\epsilon = 1.26$ and $\alpha = 1.6$, obtained by both analysis methods are slightly smaller yet close to the exponents predicted by the mean-field theory[13,14,53] and are in the range of exponent values commonly observed in experimental works.[13,37,38,54] The obtained exponent $\tau = 0.8$ differs from theoretical predictions and experimental observations.[13,14,53] The obtained cutoff values are relatively small and are approximately in the middle range of the measured variables. This issue is discussed in the next sections.

5. Discussion

5.1. The Scales of Twin Boundary Displacements and Energies during Avalanches

The measured values of the transformed volumes allow us to estimate the scales of twin boundary displacements during avalanches. At scales larger than the atomistic scale, twin boundaries lay on preferred crystallographic orientations and tend to move roughly as flat planes.[2,8,55] The force measurements captured stress drop avalanches with transformed volumes in the range of 5×10^{-11} m$^3 \leq V_T^F \leq 4 \times 10^{-9}$ m^3. Such events can be obtained by a motion of the entire twin boundary area ($A_{TB} = 10^{-5}$ m^2) as a flat plane for a distance of 5 – 400 µm.

Our results show that each stress drop avalanche is composed of numerous smaller and faster avalanches captured by the ME measurements. The largest value of V_T^{ME} observed in Figure 6a is 2.5×10^{-13} m^3. Such event can still be obtained by a motion of the entire twin boundary area for a distance of 25 nm. In contrast, events with V_T values smaller than 4×10^{-15} m^3, which constitute ≈60% of the data (see Figure 6a), cannot be explained by a motion of the entire twin boundary as a flat plane, as this scenario results in a twin boundary displacement smaller than a single lattice spacing (0.4 nm). Thus, most of the measured ME avalanches relate to motions of a small fraction of the twin boundary for distances at the nanometer scale.

The transformed volume values measured by the ME sensor are in the range of 5×10^{-16} m$^3 \leq V_T^{ME} \leq 5 \times 10^{-13}$ m^3, and are still larger by at least nine orders of magnitude than transformed volumes generated by thermally activated nucleation events (≈5×10^{-25} m^3, according to ref. [45]) by which the twin boundary propagates. A similar gap also exists between the energies $E^{ME} \geq 1.5 \times 10^{-11}$ J released during the ME avalanches ($E^{ME} = V_T^{ME} \bar{\sigma} \varepsilon_T$ where $\bar{\sigma} \approx 0.5$ MPa is an average stress and $\varepsilon_T \approx 0.06$ is the twinning strain) and the energies of thermal fluctuations $k_B T \approx 4.1 \times 10^{-21}$ J at room temperature (where k_B is the Boltzmann constant and T is the temperature).

As each stress drop avalanche is composed of numerous smaller ME avalanches and according to the above orders-of-magnitude volumetric and energetic comparison, we expect that each ME avalanche is composed of numerous avalanches occurring at even smaller energy and time scales, which are below the detection limit of ME measurements. This conjecture is supported by the idea of self-similarity, which is fundamental in many theoretical works explaining power law distributions.[13,14] The above energy estimations indicate that there is a wide range of ten orders of magnitude for additional hierarchies of avalanches with energies smaller than the ones captured by the ME measurements yet larger than $k_B T$.

5.2. The Cutoff Values

Cutoffs of power law distributions may originate from various reasons. The most common reason is the finite number of data points, which results in a cutoff value that is very close to the largest measured value.[30,40,57–59] Such observations are significantly different from ours in which, for some variables, the cutoff value is approximately in the middle of the range of captured events.

In theoretical models for classical criticality, a cutoff is expected to appear due to a deviation of the ratio R between the strengths of the disorder and the long-range interactions (see, e.g., ref. [13]). At the critical ratio (e.g., $R_c = 2.16$ in a unitless model[13]) avalanches are found over all scales resulting in a power law distribution. For $R > R_c$, avalanche sizes are limited by a cutoff that decreases as the deviation from R_c increases. However, classical criticality is more typical to force controlled ("soft" driving) mechanical experiments and is less expected to occur under displacement controlled ("hard" driving) conditions, such as those applied in our experiments.[50,60] Therefore, it is less likely that the cutoffs in our data can be explained by classical criticality.

Here, we suggest that two of the cutoff values $t_{duration}^C$ and $\dot{V}_{T,max}^C$ represent characteristics of the studied process. The third cutoff value, V_T^C, is determined by these two cutoffs, as $V_T^C \approx \dot{V}_{T,max}^C \cdot t_{duration}^C$. We note that the value of $t_{duration}^C = 9.1 \times 10^{-6}$ s is close to the time required for the elastic waves to travel along half the crystal's length, which is ≈1.25×10^{-5} s (assuming a shear wave speed of 790 m s^{-1}[61]). This traveling wave time represents the time it takes the information about a local twinning transformation event to reach the majority of the crystal volume. This characteristic time also determines the time required for the mechanical system to relax at the new metastable state. These understandings lead us to suggest that the traveling wave time provides a rough cutoff for the durations of most events.

In the following, we suggest that the cutoff $\dot{V}_{T,max}^C$ is related to the maximal twin boundary velocity determined by the kinetic relation for twin boundary motion. In the previous subsection, we showed that the energies of ME avalanches are larger by ten orders of magnitude than energies of thermal fluctuations. Therefore, it is unlikely that energy barriers for initiation of ME events are at the order of thermal activations. Nevertheless, after an ME avalanche has begun, its rate $\dot{V}_T$ may be bounded by the thermally activated kinetics of twin boundary motion over the lattice barriers.[24,43,62]

Figure 8 presents measurements of the average twin boundary velocity, v_{TB}, during rapid magnetic pulses of approximately constant field and durations of 40 or 120 µs[24] (a slightly longer, but similar, timescale as of the ME avalanches

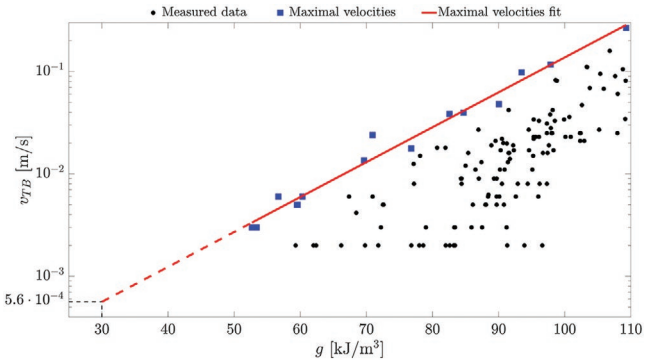

Figure 8. The black dots represent measurements of type I twin boundary velocities, v_{TB}, during magnetic pulses of different driving forces, g. The blue squares are the maximal velocities for different values of g and their linear fit is given by the red solid line. The red dashed line shows the extrapolation of the fit to the value $g = 30$ kJ m^{-3}, which is approximately the driving force in our experiments. Data is adapted with permission.[24] Copyright 2013, Elsevier.

observed in our study). These experiments were carried out on type I twin boundaries in the same Ni-Mn-Ga material as the one studied in this paper. Inertia effects associated with twin boundary acceleration have been shown to be negligible in this study.[63] The horizontal axis in Figure 8 presents the magnetically induced driving force, g, for twin boundary motion. In our study, the stress induced driving force for twin boundary motion is given by $g = \sigma\varepsilon_T \approx 30$ kJ m^{-3}.

For a given driving force value, the data in Figure 8 is scattered over 1–2 orders of magnitude due to pinning effects.[24,43,62] This means that the twin boundary did not move at a constant velocity during the pulse duration. Instead, during part of the pulse duration, the twin boundary was pinned or slowed down by local defects. Thus, the twin boundary motion at the microsecond timescale was comprised of short times at which the twin boundary moved at the maximal rate determined by the lattice scale kinetic relation, separated by time intervals at which the twin boundary was pinned. This behavior has also been demonstrated directly by high speed imaging of the twin boundary motion.[64]

Out of the measured data, the maximal velocity values captured at given driving forces $v_{TB}^{C}(g)$ are marked by blue squares in Figure 8. These values represent the behavior of an "ideal" (defect free) crystal, at which the twin boundary velocity is determined solely by the lattice barriers.[24,43,62] Under such conditions, the twin boundary motion follows an exponential kinetic relation governed by thermal activation.[24,43,62] The red solid line denotes a linear fit to the maximal velocity points (blue squares) and its extension (red dashed line) is an extrapolation that reaches the value $g = 30$ kJ m^{-3}. According to Figure 8, the maximal twin boundary velocity at the driving force applied in our experiments is expected to be v_{TB}^{C} (30 kJ m^{-3}) = 5.6×10^{-4} m s^{-1}. This value is very close to the average twin boundary velocity calculated by $\dot{V}_{T,max}^{C}/A_{TB} = 5.3 \times 10^{-4}$ m s^{-1}.

In light of the agreement between $\dot{V}_{T,max}^{C}$ measured in our experiments and v_{TB}^{C} obtained from high rate pulse experiments, we suggest that the cutoff value $\dot{V}_{T,max}^{C}$ relates to avalanches during which $\dot{V}_{T,max}$ is bounded by v_{TB}^{C}. That is, avalanches with $\dot{V}_{T,max} \leq \dot{V}_{T,max}^{C}$ correspond to events involving twin boundary motion at velocity determined by the kinetic relation ($v_{TB}^{C}(g)$) and short waiting times (much shorter than the ME temporal resolution) during which the twin boundary is pinned. We note that the $\dot{V}_{T,max}$ values that are larger than the cutoff may correspond to events with higher driving force (higher stress).

6. Conclusions

The combination of simultaneous measurements of force and ME have been demonstrated to provide insightful data. The experiments were applied to the study of twin boundary motion in the FSMA Ni-Mn-Ga during slow compression. The experimental conditions were carefully designed to eliminate the effect of "ordinary" magnetic domain switching, such that the measured ME voltage is approximately proportional to $\dot{V}_T$, where V_T is the volume undergoing twinning transformation due to the motion of a single twin boundary. Indeed, our analysis showed that the values of V_T calculated based on ME signals are in excellent correlation with the V_T values calculated based on stress drops. Thus, to a good approximation, the measured ME is directly related to local twin boundary motions at the nanometer and microsecond scales.

The variables V_T, $\dot{V}_{T,max}$, $t_{duration}$, and t_{delay} have been calculated for each of the detected ME avalanches, and their distributions have been investigated. The distributions of V_T, $\dot{V}_{T,max}$, and $t_{duration}$ related to avalanches occurring during stress drops and between stress drops coincide with each other over more than 99% of the data. These results indicate that the same microscale processes occur both during and between stress drops. At the same time, the distribution of t_{delay} of avalanches occurring during stress drops is shifted toward shorter times by 1.5–2 orders of magnitude with respect to the distribution of t_{delay} of avalanches occurring between stress drops. This means that the rate of avalanche occurrence is much higher during stress drops.

Two different approaches based on the maximum likelihood method showed that the distributions of V_T, $\dot{V}_{T,max}$, and $t_{duration}$ fit well to power laws truncated by exponential functions. The cutoff values were found to be in the middle of the detected avalanches' range, resulting in a strong effect of the exponential functions on the PDFs, even in ranges smaller than the cutoff values. We suggested physical explanations for the source of all cutoff values. Specifically, $t_{duration}^{C}$ was related to the time required for the elastic waves to travel along the sample, $\dot{V}_{T,max}^{C}$ was related to the kinetic relation for twin boundary motion over the lattice barriers, and V_T^{C} was related to the product of $t_{duration}^{C}$ and $\dot{V}_{T,max}^{C}$.

The remarkable match of $\dot{V}_{T,max}^{C}$ measured in our experiments and v_{TB}^{C} obtained from fast magnetic pulse tests implies that the same type of jerky twin boundary motion occurs both under pulses of large driving forces and under slow rate tests at small driving forces. Similar behavior was demonstrated at much smaller length and time scales, using molecular dynamics simulations. Specifically, twinning reorientation in a ferroelastic material displayed the same microstructural evolutions and avalanche distributions under a broad range of strain rates.[65] In our study, the jerky motion

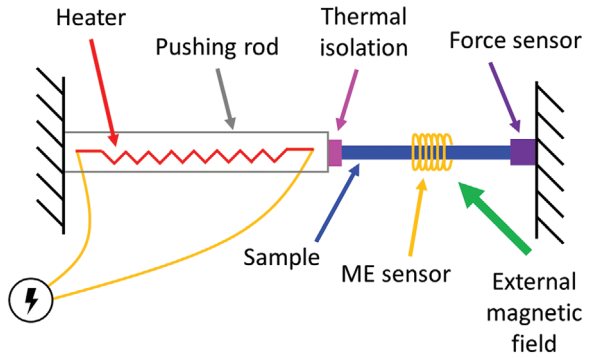

Figure 9. Illustration of the experimental setup, which is based on slow sample compression due to thermal expansion of the pushing rod. The force applied to the sample, as well as its magnetic emission (ME), are simultaneously measured throughout the experiment. An external magnetic field is applied to the sample such that the microstructural configuration illustrated in Figure 1b is achieved.

is composed of events at which the twin boundary velocity is determined by the kinetic relation, characterized by $v_{\mathrm{TB}}^{\mathrm{C}}(g)$ or $\dot{V}_{\mathrm{T,max}}^{\mathrm{C}}(g)$, followed by delay times, which are distributed over more than five decades (see Figure 5d). Events separated by delay times shorter than the temporal resolution of the measurement system are merged into one detected avalanche in slow rate tests or averaged in high rate tests. In line with this description, we showed that avalanches detected by stress drops are composed of numerous smaller and faster ME avalanches that are below the detection capability of the force sensor. Further, our analysis implies that there are additional unexplored hierarchies of avalanches with sizes and durations that are smaller than the detection capabilities of the ME sensor but much larger than typical values for thermally activated nucleation events.

The above unified description of the nature of twin boundary motion at both slow and high rates calls for further studies aimed at formulating a unified theory for the twin boundary motion at all scales and rates.

7. Experimental Section

The experimental setup is illustrated in **Figure 9** and is based on a slow uniaxial sample compression induced by thermal expansion of a 1.2 m aluminum rod (tube) with a heater inside of it. A small and stiff thermally isolating device was placed between the pushing rod and the sample. The heater was connected to a temperature control circuit that enabled a constant heating of the rod and, consequently, a constant displacement of the rod's edge. Eventually, the sample was compressed at a constant rate of $c = 2\ \mu\mathrm{m\ s^{-1}}$.

The other end of the sample was in contact with a force sensor, such that the force applied to the sample was captured during the experiment. The force sensor (Kistler 9215A) had a resolution of 1 mN and a natural frequency higher than 50 kHz; hence, it had the ability of capturing events at the sub-millisecond scale. The signal of the force sensor was amplified by a Kistler 5015 amplifier, which was connected to a NI PCI 6071E data acquisition (DAQ) card. The force channel was acquired at a rate of 10 kSa $\mathrm{s^{-1}}$.

A sensing coil (ME sensor) recorded the magnetic activity of the material throughout the experiment. The coil was made of a copper wire of 50 µm diameter and was wrapped around the sample $N = 200$ times. To prevent the coil's movement during experiments, it was covered with a Teflon tape. The sample and the coil were placed inside a polymethyl methacrylate (PMMA) holder that fixed the coil with respect to the sample yet allowed the sample to elongate freely. The magnetic signal was amplified by a dedicated amplifier with gain of 655. The amplified signal was transferred to a NI PCI 6111 DAQ card and was acquired at 4 MSa $\mathrm{s^{-1}}$. The two DAQ cards were synchronized by a preliminary electrical test, resulting in a time accuracy better than 0.25 µs.

Supporting Information

Supporting Information is available from the Wiley Online Library or from the author.

Acknowledgements

This research was supported by the United States–Israel Binational Science Foundation (BSF grant No. 2016662), by the Pazy Foundation (grant No. 78-2018), by the GINOP-2.3.2-15-2016-00041 project (co-financed by the European Union and the European Regional Development Fund), and by the Hungarian National Research, Development and Innovation Office NKFIH PD131784 project.

Conflict of Interest

The authors declare no conflict of interest.

Data Availability Statement

The data that support the findings of this study are available from the corresponding author upon reasonable request.

Keywords

avalanches, Barkhausen noise, materials mechanics, shape memory alloys, twin boundary

Received: July 8, 2021
Revised: August 25, 2021
Published online: September 17, 2021

[1] J. W. Christian, S. Mahajan, *Prog. Mater. Sci.* **1995**, *39*, 1.
[2] E. Salje, *Ferroelectrics* **1990**, *104*, 111.
[3] M. A. Meyers, A. Mishra, D. J. Benson, *Prog. Mater. Sci.* **2006**, *51*, 427.
[4] Y. Zhu, X. Liao, X. Wu, *Prog. Mater. Sci.* **2012**, *57*, 1.
[5] R. J. Asaro, P. Krysl, B. Kad, *Philos. Mag. Lett.* **2003**, *83*, 733.
[6] A. Lai, Z. Du, C. L. Gan, C. A. Schuh, *Science* **2013**, *341*, 1505.
[7] R. J. Harrison, S. A. Redfern, *Phys. Earth Planet. Inter.* **2002**, *134*, 253.
[8] K. Bhattacharya, *Microstructure of Martensite: Why It Forms and How it Gives Rise to the Shape-Memory Effect*, vol. 2, Oxford University Press, Oxford **2003**.
[9] M. Kohl, B. Krevet, S. Yeduru, Y. Ezer, A. Sozinov, *Smart Mater. Struct.* **2011**, *20*, 094009.
[10] E. Burcsu, G. Ravichandran, K. Bhattacharya, *J. Mech. Phys. Solids* **2004**, *52*, 823.
[11] I. Suorsa, E. Pagounis, K. Ullakko, *Sens. Actuators, A* **2005**, *121*, 136.

[12] I. Karaman, B. Basaran, H. Karaca, A. Karsilayan, Y. Chumlyakov, *Appl. Phys. Lett.* **2007**, *90*, 172505.
[13] J. P. Sethna, K. A. Dahmen, C. R. Myers, *Nature* **2001**, *410*, 242.
[14] E. K. Salje, K. A. Dahmen, *Annu. Rev. Condens. Matter Phys.* **2014**, *5*, 233.
[15] X. Ding, Z. Zhao, T. Lookman, A. Saxena, E. Salje, *Adv. Mater.* **2012**, *24*, 5385.
[16] S. Puchberger, V. Soprunyuk, W. Schranz, A. Tröster, K. Roleder, A. Majchrowski, M. A. Carpenter, E. K. H. Salje, *APL Mater.* **2017**, *5*, 046102.
[17] D. Soto-Parra, X. Zhang, S. Cao, E. Vives, E. K. Salje, A. Planes, *Phys. Rev. E* **2015**, *91*, 060401.
[18] L. Daróczi, E. Piros, L. Z. Tóth, D. L. Beke, *Phys. Rev. B* **2017**, *96*, 014416.
[19] B. Casals, G. F. Nataf, D. Pesquera, E. K. Salje, *APL Mater.* **2020**, *8*, 011105.
[20] E. Salje, D. Xue, X. Ding, K. A. Dahmen, J. Scott, *Phys. Rev. Mater.* **2019**, *3*, 014415.
[21] R. Flippen, *J. Appl. Phys.* **1975**, *46*, 1068.
[22] W. J. Merz, *Phys. Rev.* **1954**, *95*, 690.
[23] M. Hayashi, *J. Phys. Soc. Jpn.* **1973**, *34*, 1240.
[24] E. Faran, D. Shilo, *J. Mech. Phys. Solids* **2013**, *61*, 726.
[25] A. Mizrahi, D. Shilo, E. Faran, *Shape Memory and Superelasticity* **2020**, *6*, 45.
[26] N. Zreihan, E. Faran, E. Vives, A. Planes, D. Shilo, *Phys. Rev. B* **2018**, *97*, 014103.
[27] N. Daphalapurkar, J. Wilkerson, T. Wright, K. Ramesh, *Acta Mater.* **2014**, *68*, 82.
[28] V. Kannan, K. Hazeli, K. Ramesh, *J. Mech. Phys. Solids* **2018**, *120*, 154.
[29] A. Luque, M. Ghazisaeidi, W. A. Curtin, *Acta Mater.* **2014**, *81*, 442.
[30] N. Zreihan, E. Faran, E. Vives, A. Planes, D. Shilo, *Phys. Rev. Mater.* **2019**, *3*, 043603.
[31] J. Baró, Á. Corral, X. Illa, A. Planes, E. K. Salje, W. Schranz, D. E. Soto-Parra, E. Vives, *Phys. Rev. Lett.* **2013**, *110*, 088702.
[32] B. Casals, K. A. Dahmen, B. Gou, S. Rooke, E. K. Salje, *Sci. Rep.* **2021**, *11*, 5590.
[33] E. Salje, E. Dul'Kin, M. Roth, *Appl. Phys. Lett.* **2015**, *106*, 152903.
[34] A. Planes, L. Mañosa, E. Vives, *J. Alloys Compd.* **2013**, *577*, S699.
[35] G. Zheng, M. Buckley, G. Kister, G. Fernando, *AIAA J.* **2001**, *39*, 1198.
[36] G. K. Kocur, *J. Sound Vib.* **2017**, *387*, 66.
[37] L. Daróczi, S. Gyöngyösi, L. Z. Tóth, S. Szabó, D. L. Beke, *Appl. Phys. Lett.* **2015**, *106*, 041908.
[38] L. Daróczi, S. Gyöngyösi, L. Z. Tóth, D. L. Beke, *Scr. Mater.* **2016**, *114*, 161.
[39] B. Alessandro, C. Beatrice, G. Bertotti, A. Montorsi, *J. Appl. Phys.* **1990**, *68*, 2901.
[40] S. Zapperi, P. Cizeau, G. Durin, H. E. Stanley, *Phys. Rev. B* **1998**, *58*, 6353.
[41] E. Faran, I. Benichou, S. Givli, D. Shilo, *J. Appl. Phys.* **2015**, *118*, 244104.
[42] L. Straka, O. Heczko, H. Seiner, N. Lanska, J. Drahokoupil, A. Soroka, S. Fähler, H. Hänninen, A. Sozinov, *Acta Mater.* **2011**, *59*, 7450.
[43] E. Faran, D. Shilo, *Mater. Sci. Technol.* **2014**, *30*, 1545.
[44] E. Faran, E. K. Salje, D. Shilo, *Appl. Phys. Lett.* **2015**, *107*, 071902.
[45] E. Faran, D. Shilo, in *Avalanches in Functional Materials and Geophysics* (Eds: E. K. H. Salje, A. Saxena, A. Planes), Springer, Belin, Heidelberg **2017**, pp. 167–198.
[46] S. J. Murray, M. Marioni, S. Allen, R. O'handley, T. A. Lograsso, *Appl. Phys. Lett.* **2000**, *77*, 886.
[47] L. Straka, O. Heczko, *J. Appl. Phys.* **2003**, *93*, 8636.
[48] H. Bauke, *Eur. Phys. J. B* **2007**, *58*, 167.
[49] A. Clauset, C. R. Shalizi, M. E. Newman, *SIAM Rev.* **2009**, *51*, 661.
[50] E. Vives, D. Soto-Parra, L. Mañosa, R. Romero, A. Planes, *Phys. Rev. B* **2009**, *80*, 180101.
[51] L. Carrillo, J. Ortín, *Phys. Rev. B* **1997**, *56*, 11508.
[52] E. K. Salje, A. Planes, E. Vives, *Phys. Rev. E* **2017**, *96*, 042122.
[53] K. A. Dahmen, in *Avalanches in Functional Materials and Geophysics* (Eds: E. K. H. Salje, A. Saxena, A. Planes), Springer, Belin, Heidelberg **2017**, pp. 19–30.
[54] D. Amitrano, *J. Geophys. Res.: Solid Earth* **2003**, *108*, B1.
[55] E. Bronstein, E. Faran, D. Shilo, *Acta Mater.* **2019**, *164*, 520.
[56] J. Baró, E. Vives, *Phys. Rev. E* **2012**, *85*, 066121.
[57] Z. Balogh, L. Daróczi, L. Harasztosi, D. L. Beke, T. A. Lograsso, D. L. Schlagel, *Mater. Trans.* **2006**, *47*, 631.
[58] L. Z. Tóth, S. Szabó, L. Daróczi, D. L. Beke, *Phys. Rev. B* **2014**, *90*, 224103.
[59] D. Spasojević, S. Bukvić, S. Milošević, H. E. Stanley, *Phys. Rev. E* **1996**, *54*, 2531.
[60] F.-J. Pérez-Reche, L. Truskinovsky, G. Zanzotto, *Phys. Rev. Lett.* **2008**, *101*, 230601.
[61] L. Dai, J. Cullen, M. Wuttig, *J. Appl. Phys.* **2004**, *95*, 6957.
[62] D. Shilo, E. Faran, B. Karki, P. Müllner, *Acta Mater.* **2021**.
[63] E. Faran, D. Shilo, *J. Mech. Phys. Solids* **2011**, *59*, 975.
[64] A. Mizrahi, U. Heller, E. Faran, D. Shilo, *Exp. Mech.* **2020**, *60*, 191.
[65] L. Zhang, E. Salje, X. Ding, J. Sun, *Appl. Phys. Lett.* **2014**, *104*, 162906.